



Determining the Efficiency of Converting Magnetar Spindown Energy into Gamma-Ray Burst X-Ray Afterglow Emission and Its Possible Implications

Di Xiao^{1,2}  and Zi-Gao Dai^{1,2}¹ School of Astronomy and Space Science, Nanjing University, Nanjing 210093, People's Republic of China; dxiao@nju.edu.cn² Key Laboratory of Modern Astronomy and Astrophysics (Nanjing University), Ministry of Education, Nanjing, People's Republic of China; dzg@nju.edu.cn

Received 2019 January 29; revised 2019 March 18; accepted 2019 March 21; published 2019 June 13

Abstract

Plateaus are common in X-ray afterglows of gamma-ray bursts. Among the few scenarios regarding their origin, the leading one is that there exists a magnetar inside and it persistently injects its spindown energy into an afterglow. In previous studies, the radiation efficiency of this process is assumed to be a constant at $\gtrsim 0.1$, which is quite simple and strong. In this work we obtain the efficiency from a physical point of view and find that this efficiency strongly depends on the injected luminosity. One implication of this result is that those X-ray afterglow light curves that show steeper temporal decay than t^{-2} after the plateau phase can be naturally understood now. Also, the braking indexes deduced from afterglow fitting are found to be larger than those in previous studies, which are more reasonable for newborn magnetars.

Key words: gamma-ray burst: general – radiation mechanisms: general – stars: neutron

1. Introduction

After a tens-of-years study on gamma-ray bursts (GRBs), one mainstream viewpoint among the community is that there is a dichotomy in their central engines: either black hole (BH) accretion systems or newborn millisecond magnetars can power GRBs under certain circumstances (for a recent review, see Kumar & Zhang 2015). Unlike a BH system that usually extracts the gravitational energy of accreted matter (e.g., Woosley 1993; Popham et al. 1999; Narayan et al. 2001), a millisecond magnetar extracts its stellar rotational energy to power a GRB and its afterglow (e.g., Usov 1992; Thompson 1994; Dai & Lu 1998a, 1998b; Zhang & Mészáros 2001; Mazzali et al. 2014; Beniamini et al. 2017). Ever since the launch of the *Swift* satellite, X-ray afterglows of dozens of GRBs have been found to exhibit plateau features, which are thought to be the signature of a long-lasting energy injection from the central engine (Zhang et al. 2006). If the central engine is a BH, the injected energy could come from the fallback accretion onto the BH (Ruffert et al. 1997; Rosswog et al. 2003; Lei et al. 2013; Wu et al. 2014).³ However, the required fallback mass in the BH model may be too large to explain a plateau at late times ($>10^5$ s; Liu et al. 2017). An alternative way is to introduce a spindown energy injection from a newborn magnetar (Dai & Lu 1998a, 1998b; Zhang & Mészáros 2001), which will be discussed in detail below.

The origin of plateaus in X-ray afterglow light curves is still under debate, and basically we would expect two different kinds. The first kind is called “external plateaus” that originate from external shocks. In this case the energy injection comes from a late kinetic-energy-dominated shell interacting with a preceding expanding fireball (e.g., Panaitescu et al. 1998; Rees & Mészáros 1998), so the X-ray light curve should be related to those of other wavelengths (e.g., Dermer 2007; Genet et al. 2007; Uhm & Beloborodov 2007). The second one is “internal plateaus” that could reflect the activity of central engines (e.g., Troja et al. 2007; Yu et al. 2009, 2010; Beniamini &

Mochkovitch 2017). The most prominent feature of an internal plateau is that there is a rapid decay at the end of the plateau, usually with a temporal slope steeper than -3 (Liang et al. 2007; Lyons et al. 2010; Rowlinson et al. 2010). This sudden drop is hard to interpret with a BH central engine but can be well explained as the central magnetar collapse to a BH (Troja et al. 2007; Rowlinson et al. 2010, 2013; Lü & Zhang 2014).

Specifically within the magnetar framework, by what means a magnetar can convert its spindown energy into radiation is unsure (Usov 1999; Zhang & Mészáros 2002). If the X-ray plateau is “external,” one commonly discussed physical model is that an accelerated magnetar wind (which is ultra-relativistic, electron–positron-pair-dominated) interacts with a preceding expanding fireball or an ambient medium (Dai 2004). A relativistic “wind bubble” (which is a relativistic version of pulsar wind nebula) is formed and the reverse shock can accelerate electrons to produce multiwavelength emission (Yu & Dai 2007). If the X-ray plateau is “internal,” it can be produced by an internal energy dissipation in the magnetar wind (Coroniti 1990; Usov 1994). In this case the spindown power is mediated by an initially cold, Poynting-flux-dominated wind that can be gradually accelerated as its magnetic energy dissipates internally via magnetic reconnection (Spruit et al. 2001; Drenkhahn 2002; Drenkhahn & Spruit 2002). There will be high-energy emission in this process (Giannios & Spruit 2005; Metzger et al. 2011; Giannios 2012; Beniamini & Piran 2014; Beniamini & Giannios 2017; Xiao & Dai 2017; Xiao et al. 2018) that can be responsible for the X-ray plateau. In this work we focus on the latter case and calculate the X-ray radiation efficiency in this physical model.

A newborn magnetar loses its rotational energy via gravitational-wave and electromagnetic radiation, whose angular velocity evolution can be generalized as follows (Lasky et al. 2017):

$$\dot{\Omega} = -k\Omega^n, \quad (1)$$

where $\Omega = \Omega(t) = 2\pi/P(t)$ is the spin angular velocity, and k and n represent a constant of proportionality and the braking

³ Note that fallback accretion around a magnetar was also proposed to power GRBs (e.g., Metzger et al. 2018).

index of magnetar, respectively. The solution of Equation (1) is (Lasky et al. 2017; Lü et al. 2018)

$$\Omega(t) = \Omega_0 \left(1 + \frac{t}{\tau}\right)^{\frac{1}{1-n}}, \quad (2)$$

where Ω_0 is the initial angular velocity and $\tau \equiv \Omega_0^{1-n}/[(n-1)k]$ is the spindown timescale. The injected energy into the afterglow comes from the magnetic dipole torque whose luminosity is $L_{EM} = B^2 R^6 \Omega^4 / 6c^3 = L_0 (1 + t/\tau)^{4/(1-n)}$, where $L_0 \equiv B^2 R^6 \Omega_0^4 / 6c^3 = 1.0 \times 10^{49} B_{15}^2 R_6^6 P_{-3}^{-4}$ erg s⁻¹. Throughout this paper the notation $Q = 10^x Q_x$ in cgs units is adopted and the radius of magnetar is assumed to be $R = 10^6$ cm. The observed X-ray plateau luminosity is $L_X = \eta_X L_{EM}$ by introducing an efficiency η_X , where η_X could evolve with time. A bunch of X-ray afterglow light curves with plateau features have been well fitted within the magnetar energy injection scenario, however, all by assuming that η_X is constant (e.g., Lasky et al. 2017; Lü et al. 2018). We think better of this assumption in this work.

This paper is organized as follows. In Section 2 we calculate the X-ray radiation efficiency and obtain its relation on the injected luminosity. Section 3 presents the impact of the above relation on afterglow fitting, including both theoretical analysis and case fitting. We also compare our results with previous studies. We finish with conclusions and discussions in Section 4.

2. X-Ray Radiation Efficiency

The wind from a newborn rapidly rotating magnetar is initially cold and Poynting-flux-dominated (Coroniti 1990; Aharonian et al. 2012). As the wind propagates outward, its magnetic energy gradually dissipates via reconnection and is finally converted to high-energy radiation and kinetic energy of the wind. This emission is composed of a thermal component and a nonthermal synchrotron component that can be calculated in detail (Beniamini & Giannios 2017; Xiao & Dai 2017; Xiao et al. 2018). As an example, Figure 1 shows the spectrum of high-energy emission from the newborn magnetar wind with an initial magnetization $\sigma_0 = 100$. The spin period of central magnetar is assumed as $P = 1$ ms and the magnetic field strength is $B = 10^{15}$ G. Then, the X-ray luminosity can be obtained by integrating on the *Swift*-XRT band (0.3 – 10 keV), and the X-ray radiation efficiency is defined as

$$\eta_X \equiv \frac{\int_{0.3 \text{ keV}}^{10 \text{ keV}} L_\nu d\nu}{L_{EM}}. \quad (3)$$

Further, we can calculate efficiencies with other given values of P and B . For different parameter sets, different cases are named in the form of ‘‘PxBy,’’ with x denoting the spin period in ms and y denoting the logarithm of the magnetic field strength in Gauss. Other than the spin and magnetic field, the wind’s saturation Lorentz factor Γ_{sat} that is related to the initial magnetization parameter σ_0 as $\Gamma_{\text{sat}} = \sigma_0^{3/2}$ (Beniamini & Giannios 2017) also plays an important role, which has been discussed in Xiao & Dai (2017). We have calculated the efficiencies for parameter assemblies within $P = 1, 3, 5$ ms; $B = 10^{14}, 10^{15}, 10^{16}$ G; and $\Gamma_{\text{sat}} = 10^2, 10^{2.5}, 10^3, 10^4, 10^5$. The results are listed in Table 1. We carry out polynomial

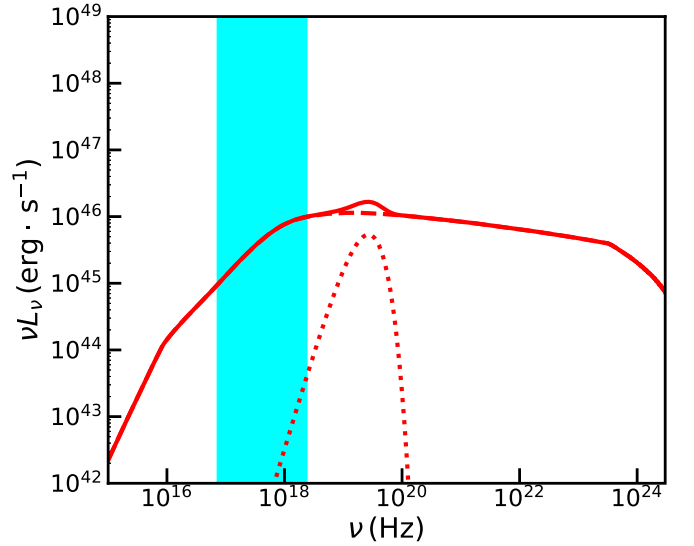


Figure 1. High-energy emission spectrum of the internal gradual magnetic energy dissipation process from the wind of a newborn magnetar with spin period $P = 1$ ms and magnetic field strength $B = 10^{15}$ G. The total spectrum (red solid line) is a sum of thermal (red dotted line) and nonthermal components (red dashed line). Cyan region represents the observational frequency range of *Swift*-XRT.

fitting to obtain the dependences of η_X on L_{EM} , which are

$$\begin{aligned} \log \eta_X &= -0.042(\log L_{EM})^2 + 3.81 \log L_{EM} - 87.29, \\ \log \eta_X &= -0.059(\log L_{EM})^2 + 5.61 \log L_{EM} - 134.60, \\ \log \eta_X &= -0.030(\log L_{EM})^2 + 3.10 \log L_{EM} - 80.28, \\ \log \eta_X &= -0.0034(\log L_{EM})^2 - 0.016 \log L_{EM} - 10.89, \\ \log \eta_X &= -0.011(\log L_{EM})^2 - 0.75 \log L_{EM} + 4.78, \end{aligned} \quad (4)$$

for $\Gamma_{\text{sat}} = 10^2, 10^{2.5}, 10^3, 10^4, 10^5$, respectively, as shown in Figure 2. As we can see clearly, the X-ray efficiency strongly depends on the injected luminosity $\eta_X = \eta_X(L_{EM})$, which will influence the X-ray light curve at late times.

3. Impact on the Temporal Decay Index after Plateau

3.1. Theoretical Analysis

Since the efficiency evolves as the injected electromagnetic luminosity decreases, we can expect that the decay index β of X-ray flux after the plateau phase ($F_X \propto t^\beta$) will deviate from the commonly believed value -2 . (e.g., Zhang & Mészáros 2001). Figure 3 shows how the X-ray light curves behave if we take the relation $\eta_X = \eta_X(L_{EM})$ into account. For three cases of $\Gamma_{\text{sat}} = 10^3, 10^4, 10^5$, as η_X decreases monotonously with decreasing L_{EM} , the temporal indexes appear $\beta < -2$ after plateau. However, for $\Gamma_{\text{sat}} = 10^2, 10^{2.5}$ cases, η_X first increases and then decreases later with decreasing L_{EM} . This leads to $\beta > -2$ above a critical value $L_{EM, \text{cr}}$ and turns into $\beta < -2$ after L_{EM} drops below this value. This break in the temporal decay index is totally caused by the evolution of η_X , and an application of this effect to individual cases needs fine-tuning and is left for future work.

In the conventional picture, if the magnetar spins down only through a dipole torque, the braking index $n = 3$. If it spins down only through gravitational-wave radiation, then $n = 5$ (Shapiro & Teukolsky 1983). For a newborn magnetar, we can

Table 1
X-Ray Radiation Efficiencies Using Different Parameter Sets

P, B	P5B14	P3B14	P1B14	P5B15	P3B15	P1B15	P5B16	P3B16	P1B16
Γ_{sat}					η_X				
$\Gamma_{\text{sat}} = 10^2$	3.99×10^{-2}	4.86×10^{-2}	2.10×10^{-2}	4.72×10^{-2}	3.20×10^{-2}	7.00×10^{-3}	2.51×10^{-2}	1.23×10^{-2}	... ^a
$\Gamma_{\text{sat}} = 10^{2.5}$	9.63×10^{-3}	1.50×10^{-2}	3.36×10^{-2}	2.57×10^{-2}	3.65×10^{-2}	1.99×10^{-2}	4.32×10^{-2}	2.96×10^{-2}	6.30×10^{-3}
$\Gamma_{\text{sat}} = 10^3$	1.28×10^{-3}	2.17×10^{-3}	7.08×10^{-3}	4.76×10^{-3}	8.01×10^{-3}	2.20×10^{-2}	1.54×10^{-2}	2.40×10^{-2}	1.98×10^{-2}
$\Gamma_{\text{sat}} = 10^4$	1.23×10^{-5}	1.90×10^{-5}	6.58×10^{-5}	4.57×10^{-5}	8.18×10^{-5}	3.03×10^{-4}	2.03×10^{-4}	3.72×10^{-4}	1.37×10^{-3}
$\Gamma_{\text{sat}} = 10^5$	1.33×10^{-7}	1.62×10^{-7}	4.83×10^{-7}	3.62×10^{-7}	6.07×10^{-7}	2.22×10^{-6}	1.50×10^{-6}	2.76×10^{-6}	1.03×10^{-5}

Note.

^a For this parameter set the saturation radius is even smaller than the photospheric radius. The high-energy emission is then totally thermalized and the model in this work does not apply.

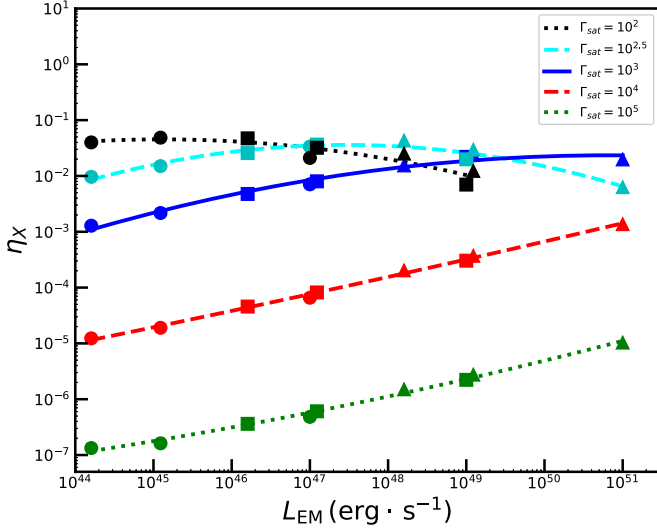


Figure 2. Polynomial fitting of the dependences of η_X on the injected luminosity L_{EM} . We consider five cases of $\Gamma_{\text{sat}} = 10^2, 10^{2.5}, 10^3, 10^4, 10^5$ that are indicated in the upper right corner. Different symbols are used to differentiate the magnetic field strength: circles, squares, and triangles are for $B = 10^{14}, 10^{15},$ and 10^{16} G, respectively.

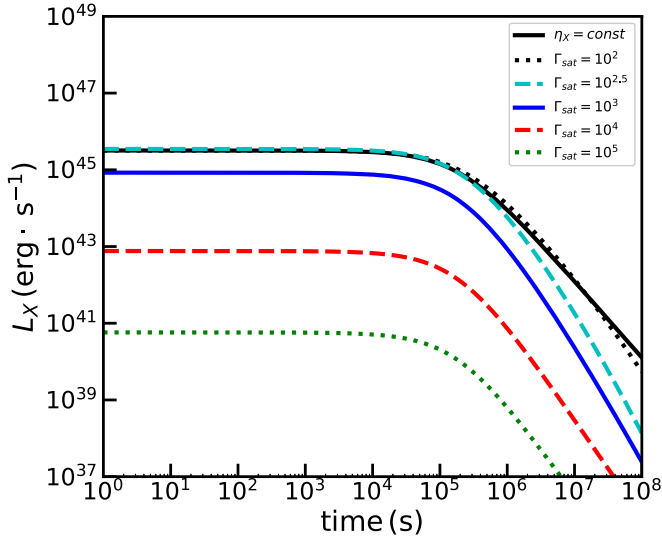


Figure 3. Theoretical X-ray light curves of magnetar energy injection. Different lines represent different Γ_{sat} indicated in the upper right corner. The black solid line represents the traditional $\eta_X = \text{const}$ assumption, and it has been normalized to the initial value of $\Gamma_{\text{sat}} = 10^2$ case. Clearly the temporal decay indexes after plateau of all five cases deviate from $\beta = -2$.

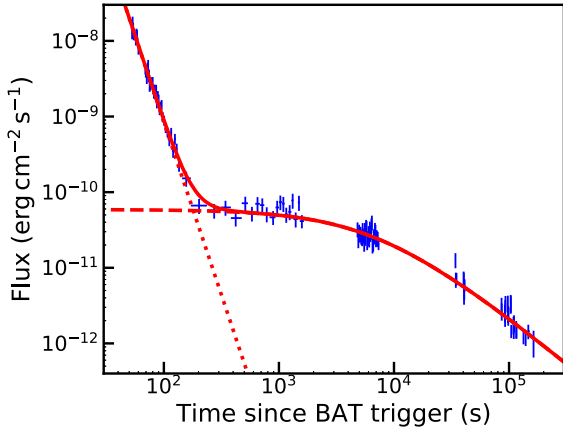
expect these two mechanisms are both very important and their combined effect on spin evolution leads to $3 \leq n \leq 5$.⁴ As long as k is constant in Equation (1), we can deduce from Equation (2) that the decay index of X-ray light curve after plateau is $\beta = 4/(1 - n)$ and should lie between -1 and -2 . However, observationally we have found a lot of cases with decay indexes $\beta < -2$. Traditionally we have to make a further assumption that k evolves with time to reconcile this discrepancy (Lasky et al. 2017). However, we have shown here that the evolution of η_X with time is a more natural explanation that should be given priority.

We can now apply our result to fit individual cases. The initial steep decay of X-ray afterglow light curve is fitted with a power-law component $L_{\text{pl}} = At^{-\alpha}$, and the observed X-ray flux is then $F_X = (1 + z)(\eta_X L_{\text{EM}} + L_{\text{pl}})/4\pi D_L^2$, where z is redshift and D_L is the corresponding luminosity distance. Note that at different redshifts the ranges of integration of Equation (3) in the burst frame vary, so that η_X should be calculated case by case. Taking $(A, \alpha, L_0, n, \tau)$ as parameters we can do a Bayesian Monte Carlo fitting using the MCMC package (Zhang et al. 2016). Figure 4 gives two examples of afterglow fitting results, which are GRB 100615A with normal $\beta > -2$ and GRB 150910A with $\beta < -2$. We can see from Figure 4(c) that the X-ray efficiencies are smaller than 0.1 and trace the time evolution of L_{EM} . For this figure and the results below, we assume $\Gamma_{\text{sat}} = 10^3$, which corresponds to initial magnetization $\sigma_0 = 100$ and is very typical for a GRB (Beniamini & Giannios 2017). The best-fitting values and parameter corners are shown in Table 2 and Figures 5 and 6. Since the power-law component can be well identified, once we fix A or α there is not much space for the other, so A and α are highly degenerated. Also, as we can see from Equation (2) and the definition below it, there is a correlation among $L_0, \tau,$ and n . Therefore, either pair of them could be moderately degenerated.

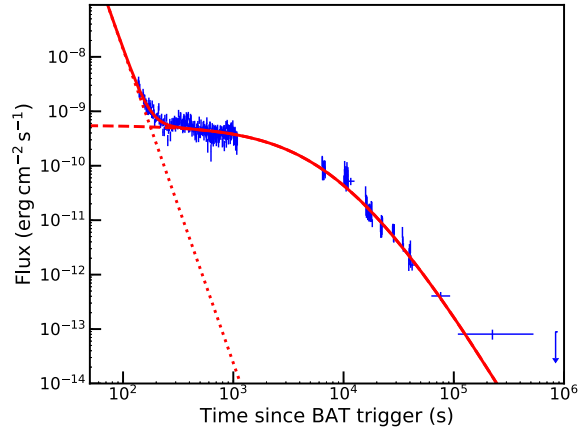
3.2. Comparison with Previous Work

Since the X-ray light curve decays faster in our analysis, the braking index deduced from afterglow fitting should also differ from previous studies. For example if $\beta = -2$, traditionally we get $n = 3$. However, as long as η_X decreases with time, in our analysis $4/(1 - n) > -2$ is required, leading to $n > 3$. Therefore, generally we will obtain larger values of n from afterglow fitting. In order to illustrate this effect directly, we adopt the same sample as in Lü et al. (2018) and compare our

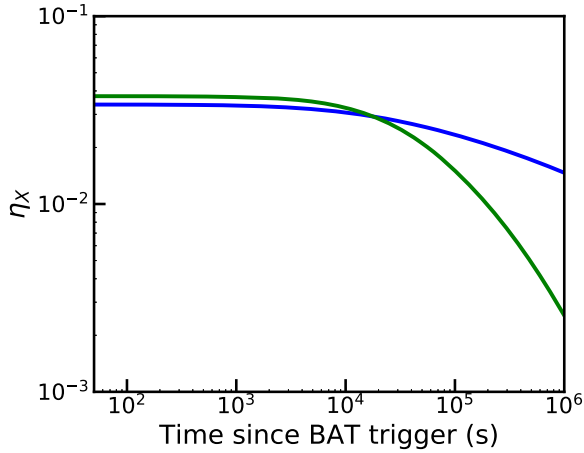
⁴ A larger range of the braking index is possible if the other mechanism is taken into account. For instance, neutron stars that spin down through unstable r-modes have $n = 7$ (Owen et al. 1998). Also, the fallback accretion could lead to $n < 3$ (Metzger et al. 2018).



(a) The fitting result of X-ray afterglow light curve for GRB 100615A.



(b) The fitting result of X-ray afterglow light curve for GRB 150910A.



(c) The X-ray efficiencies as a function of time for the above two cases: blue for GRB 100615A and green for GRB 150910A.

Figure 4. Two examples of afterglow fitting results: GRB 100615A with $\beta > -2$ and GRB 150910A with $\beta < -2$.

result with theirs, in which constant $\eta_x = 0.1$ was assumed. GRB 100615 was within that sample and their best-fitting braking index is $n = 4.61 \pm 0.14$, which is smaller than our value in Table 2. This is easy to understand from the above discussion. In fact, we have redone the fitting using our

Table 2

The Best-fitting Values for the Five Parameters Using the Bayesian Monte Carlo Method

(a) Parameters for GRB 100615A		
Parameter	Allowed Range	Best-fitting Value
$\log A$	[40, 100]	$57.77^{+0.16}_{-0.19}$
α	[0, 15]	$4.56^{+0.084}_{-0.098}$
$\log L_0$	[42, 52]	$48.97^{+0.025}_{-0.036}$
n	[1, 7]	$4.84^{+0.24}_{-0.24}$
$\log \tau$	[1, 10]	$3.78^{+0.11}_{-0.098}$
(b) Parameters for GRB 150910A		
Parameter	Allowed Range	Best-fitting Value
$\log A$	[40, 100]	$61.07^{+0.88}_{-0.60}$
α	[0, 15]	$5.63^{+0.40}_{-0.27}$
$\log L_0$	[42, 52]	$49.87^{+0.0093}_{-0.0065}$
n	[1, 7]	$2.55^{+0.082}_{-0.070}$
$\log \tau$	[1, 10]	$3.82^{+0.038}_{-0.048}$

relation, and a complete comparison of fitted parameters with Lü et al. (2018) is shown in Table 3 and the distribution of n is shown in Figure 7. Since our fitted X-ray efficiency is less than 0.1, the values of L_0 are universally larger than those in Lü et al. (2018). Moreover, we find that the deduced braking indexes are also universally larger in this work. The central position of the distribution on n is also shifted to a larger value.

A critical point we should check is whether the values of parameters chosen for fitting the X-ray plateaus are consistent with the luminosity requirements during the prompt phase of the same bursts. As we can see in Table 3, the deduced initial injected luminosity L_0 is centered near 10^{49} erg s $^{-1}$, which looks smaller than the typical prompt luminosity. However, an important uncertainty should be taken into account, which is the beaming effect. At such late times of X-ray plateau, the outflow has gone through remarkable sideways expansion and the injected luminosity is quasi-isotropic. But during the early prompt phase, the jet should be highly beamed. If we assume a double-sided jet with an opening angle ~ 0.1 , the observed luminosity during the prompt phase is then 200 times higher, which is of order 10^{51} erg s $^{-1}$ and can easily match the luminosity requirement of the prompt phase. Furthermore, there will be some correlation for the observed spectrum between the prompt and X-ray plateau phases. As we have discussed in Xiao et al. (2018), the temperature of the thermal component depends weakly on the injected luminosity ($T_{\text{ph}} \propto L_{\text{EM}}^{1/10}$ from Equation (3) in that work). Therefore, even the luminosity is 200 times lower during the X-ray plateau phase due to jet widening; the temperature is only 1.7 times lower than that of the prompt phase. Thus, we can expect that the peak energy is nearly the same in these two phases. Note that the above discussion is valid only if the prompt and X-ray plateau emissions both originate from the gradual magnetic dissipation process. If they do not have the same origin mechanism, there will be no correlation of the peak energy during these two phases. For example, if the prompt emission comes from the accretion of a newborn magnetar (e.g., Zhang & Dai 2008, 2009, 2010) or the differential rotation in the magnetar's interior (e.g., Kluźniak & Ruderman 1998; Dai & Lu 1998b), then its luminosity and spectral properties depend

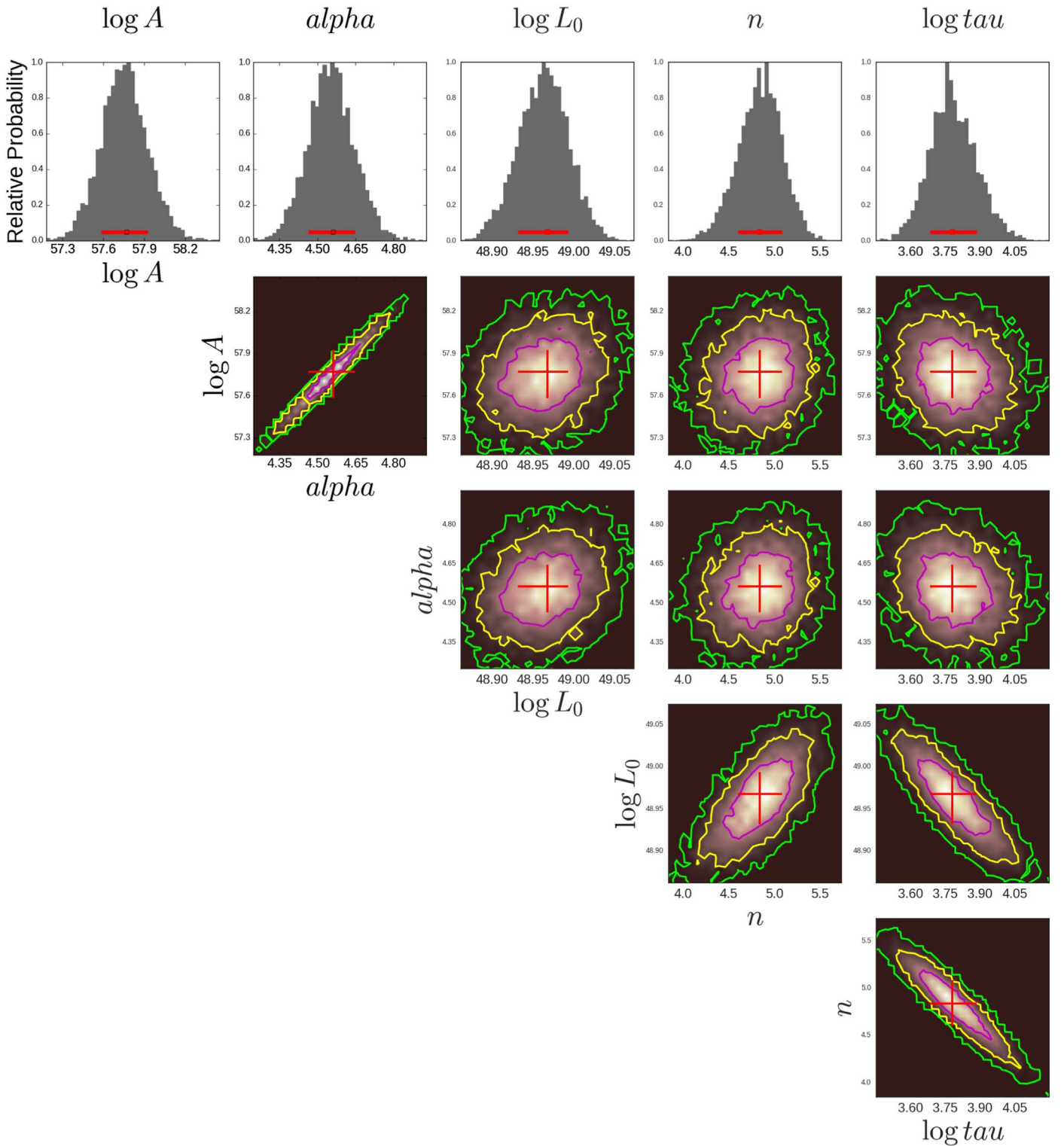


Figure 5. Parameter constraints of afterglow light-curve fitting for GRB 100615A. Histograms and contours illustrate the likelihood map. Red crosses show the best-fitting values and 1σ error bars.

on the mass accretion rate or the differentially rotational energy.

4. Conclusions and Discussion

In this work we have revisited the scenario that a GRB X-ray afterglow is powered by a continuous energy injection of a newborn magnetar. Generally we would expect to test the

internal magnetic dissipation model via spectral evolution from observations. For the canonical parameters used in Figure 1, at the beginning the observed frequency of *Swift*-XRT satisfies $\nu_c < \nu_a < \nu_{\text{XRT}} < \nu_m$, and then turns into $\nu_a < (\nu_m, \nu_{\text{XRT}}) < \nu_c$ quickly. As indicated by Equations (14)–(16) of our previous work (Xiao & Dai 2017), at the beginning the X-ray spectrum should be $L_\nu \propto \nu^{-0.5}$ and becomes $L_\nu \propto$

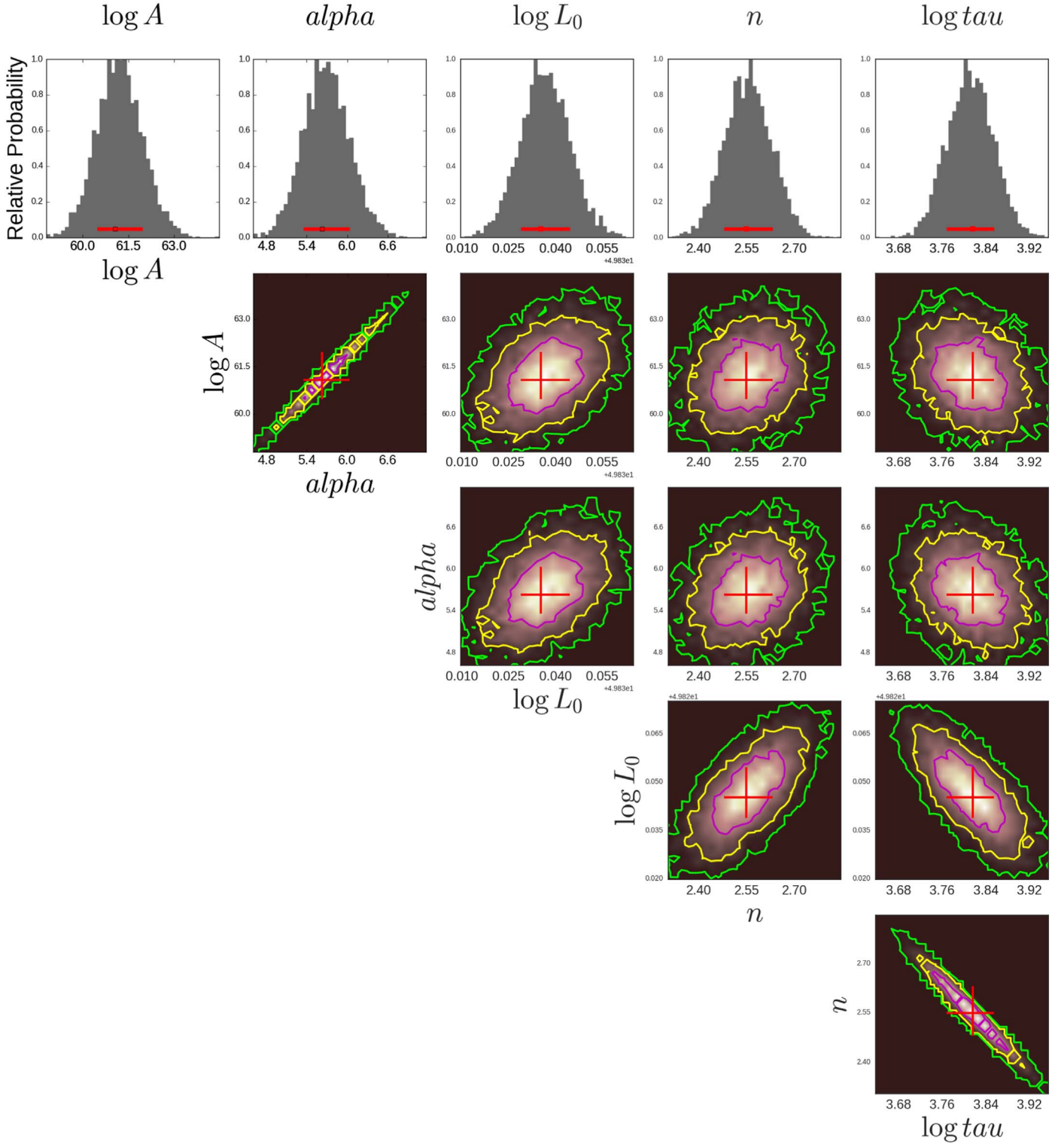


Figure 6. Same as Figure 5, but for GRB 150910A.

$\nu^{-(p-1)/2}$ later. To identify this spectral evolution from observations, we need the spectrum measurement at very early times (at the beginning of the plateau phase); otherwise, the spectral index has become $-(p-1)/2$. For the power-law component that has an external origin, the X-ray spectral index should be $-(p-1)/2$ or $-p/2$, depending on whether the electrons accelerated by external shocks are in a slow or fast cooling regime. For most of the cases in XRT archival data, the

X-ray spectral indexes are around $-(p-1)/2$ during the plateau phase and it is not easy to test the model. However, we still have some special cases like GRB 061121, whose X-ray photon index shows a clear transition from 1.46 ± 0.03 at $T_0 + 173$ s (very close to the beginning of plateau phase) to 1.83 ± 0.06 at $T_0 + 20872$ s (Evans et al. 2009). This spectral evolution from ~ -0.5 to $-(p-1)/2$ strongly favors the model presented in this work. Moreover, a general prediction of

Table 3
The Comparison on the Parameters Deduced in This Work and Lü et al. (2018)

GRB	log A	α	log L_0		n		log τ	
			This Work	Lü et al. (2018)	This Work	Lü et al. (2018)	This Work	Lü et al. (2018)
050319	53.79 ^{+6.63} _{-0.77}	2.20 ^{+2.62} _{-0.30}	48.92 ^{+0.11} _{-0.04}	47.81 ± 0.01	3.88 ^{+0.50} _{-0.25}	4.14 ± 0.14	4.25 ^{+0.10} _{-0.28}	3.87 ± 0.04
050822	74.97 ^{+3.22} _{-2.56}	9.72 ^{+1.17} _{-0.92}	48.30 ^{+0.03} _{-0.05}	46.65 ± 0.01	5.35 ^{+0.12} _{-0.15}	4.45 ± 0.11	3.92 ^{+0.10} _{-0.06}	4.12 ± 0.04
050922B	77.54 ^{+1.06} _{-0.77}	9.44 ^{+0.35} _{-0.25}	48.12 ^{+0.04} _{-0.04}	46.87 ± 0.02	3.30 ^{+0.36} _{-0.28}	2.94 ± 0.26	5.29 ^{+0.11} _{-0.15}	5.30 ± 0.14
051016B	61.28 ^{+1.70} _{-1.66}	6.89 ^{+0.86} _{-0.84}	47.87 ^{+0.04} _{-0.04}	46.12 ± 0.001	4.67 ^{+0.16} _{-0.19}	3.80 ± 0.13	3.98 ^{+0.09} _{-0.08}	4.14 ± 0.05
060604	70.71 ^{+0.90} _{-0.58}	9.39 ^{+0.39} _{-0.25}	48.37 ^{+0.05} _{-0.04}	47.02 ± 0.02	4.51 ^{+0.22} _{-0.15}	4.04 ± 0.13	4.06 ^{+0.08} _{-0.12}	4.03 ± 0.05
060605	53.74 ^{+1.78} _{-0.82}	2.58 ^{+0.86} _{-0.39}	49.18 ^{+0.05} _{-0.05}	48.04 ± 0.01	2.47 ^{+0.15} _{-0.17}	2.48 ± 0.08	4.09 ^{+0.11} _{-0.10}	3.95 ± 0.04
060714	81.45 ^{+0.85} _{-1.38}	14.05 ^{+0.37} _{-0.61}	49.16 ^{+0.02} _{-0.04}	47.78 ± 0.02	4.46 ^{+0.08} _{-0.16}	3.86 ± 0.10	3.34 ^{+0.10} _{-0.05}	3.49 ± 0.05
060729	60.94 ^{+0.09} _{-0.09}	5.39 ^{+0.04} _{-0.04}	47.99 ^{+0.01} _{-0.01}	46.24 ± 0.0005	3.94 ^{+0.05} _{-0.04}	3.34 ± 0.03	4.92 ^{+0.01} _{-0.02}	4.96 ± 0.01
061121	60.71 ^{+0.13} _{-0.10}	5.52 ^{+0.06} _{-0.05}	49.54 ^{+0.01} _{-0.01}	48.16 ± 0.01	4.09 ^{+0.04} _{-0.03}	3.71 ± 0.03	3.47 ^{+0.02} _{-0.02}	3.45 ± 0.01
070129	70.22 ^{+0.31} _{-0.25}	7.57 ^{+0.11} _{-0.09}	48.22 ^{+0.02} _{-0.03}	46.85 ± 0.01	4.40 ^{+0.13} _{-0.17}	3.95 ± 0.12	4.40 ^{+0.08} _{-0.06}	4.31 ± 0.04
070306	64.64 ^{+0.21} _{-0.29}	6.67 ^{+0.09} _{-0.12}	48.66 ^{+0.01} _{-0.01}	47.17 ± 0.01	2.69 ^{+0.09} _{-0.12}	2.38 ± 0.08	4.81 ^{+0.06} _{-0.04}	4.86 ± 0.04
070328	63.79 ^{+1.80} _{-1.76}	7.37 ^{+0.91} _{-0.86}	50.69 ^{+0.01} _{-0.01}	49.34 ± 0.004	3.51 ^{+0.03} _{-0.03}	3.33 ± 0.02	2.79 ^{+0.02} _{-0.02}	2.83 ± 0.01
070508	70.35 ^{+5.10} _{-9.47}	13.22 ^{+0.29} _{-8.52}	50.06 ^{+0.01} _{-0.01}	48.51 ± 0.003	4.02 ^{+0.03} _{-0.03}	3.56 ± 0.02	2.64 ^{+0.02} _{-0.02}	2.79 ± 0.01
080430	52.99 ^{+0.19} _{-0.30}	2.62 ^{+0.10} _{-0.15}	48.00 ^{+0.03} _{-0.03}	46.44 ± 0.02	5.27 ^{+0.14} _{-0.09}	4.68 ± 0.07	3.96 ^{+0.06} _{-0.07}	3.76 ± 0.03
081210	54.52 ^{+0.87} _{-0.53}	2.35 ^{+0.32} _{-0.19}	48.00 ^{+0.04} _{-0.08}	46.45 ± 0.02	3.93 ^{+0.92} _{-0.65}	3.34 ± 0.33	4.63 ^{+0.27} _{-0.44}	4.72 ± 0.14
090404	64.85 ^{+0.10} _{-0.10}	7.01 ^{+0.05} _{-0.05}	48.64 ^{+0.01} _{-0.03}	47.31 ± 0.01	4.13 ^{+0.08} _{-0.15}	3.63 ± 0.11	4.25 ^{+0.07} _{-0.03}	4.30 ± 0.04
090516	80.96 ^{+1.35} _{-0.98}	12.44 ^{+0.55} _{-0.39}	50.85 ^{+0.30} _{-0.10}	48.05 ± 0.01	4.28 ^{+0.07} _{-0.04}	2.81 ± 0.07	2.22 ^{+0.10} _{-0.30}	4.09 ± 0.03
090529	57.43 ^{+0.18} _{-0.22}	3.55 ^{+0.08} _{-0.09}	47.61 ^{+0.11} _{-0.08}	46.02 ± 0.04	5.25 ^{+1.10} _{-0.74}	4.03 ± 0.62	4.42 ^{+0.29} _{-0.43}	4.69 ± 0.27
090618	62.75 ^{+0.14} _{-0.11}	5.97 ^{+0.06} _{-0.05}	49.56 ^{+0.01} _{-0.01}	47.96 ± 0.002	4.38 ^{+0.02} _{-0.02}	3.82 ± 0.01	3.04 ^{+0.02} _{-0.02}	3.16 ± 0.01
091018	61.86 ^{+2.89} _{-17.69}	8.17 ^{+5.21} _{-3.23}	49.65 ^{+0.04} _{-0.01}	48.13 ± 0.01	4.68 ^{+0.08} _{-0.03}	4.12 ± 0.04	2.39 ^{+0.02} _{-0.08}	2.51 ± 0.03
091029	63.47 ^{+3.56} _{-1.31}	6.08 ^{+1.41} _{-0.51}	48.68 ^{+0.03} _{-0.03}	47.32 ± 0.01	4.65 ^{+0.14} _{-0.08}	4.08 ± 0.09	3.99 ^{+0.03} _{-0.07}	4.05 ± 0.03
100302A	62.56 ^{+0.45} _{-0.26}	5.16 ^{+0.17} _{-0.10}	48.10 ^{+0.10} _{-0.06}	46.83 ± 0.02	5.83 ^{+0.48} _{-0.38}	5.05 ± 0.26	4.03 ^{+0.16} _{-0.25}	4.06 ± 0.09
100615A	57.77 ^{+0.16} _{-0.19}	4.56 ^{+0.08} _{-0.10}	48.97 ^{+0.03} _{-0.04}	47.55 ± 0.01	4.84 ^{+0.24} _{-0.24}	4.61 ± 0.14	3.78 ^{+0.11} _{-0.10}	3.65 ± 0.05
100814A	60.83 ^{+0.21} _{-0.13}	4.83 ^{+0.09} _{-0.05}	48.54 ^{+0.02} _{-0.02}	47.11 ± 0.01	3.24 ^{+0.07} _{-0.10}	3.02 ± 0.06	4.96 ^{+0.05} _{-0.04}	4.85 ± 0.02
110808A	56.62 ^{+0.33} _{-0.26}	3.91 ^{+0.16} _{-0.12}	47.47 ^{+0.12} _{-0.07}	45.87 ± 0.03	5.46 ^{+0.79} _{-0.62}	4.87 ± 0.41	4.30 ^{+0.21} _{-0.37}	4.13 ± 0.15
111008A	58.42 ^{+0.20} _{-0.14}	4.13 ^{+0.10} _{-0.07}	49.61 ^{+0.02} _{-0.02}	48.41 ± 0.01	4.04 ^{+0.10} _{-0.06}	3.69 ± 0.07	3.72 ^{+0.03} _{-0.06}	3.81 ± 0.03
111228A	60.87 ^{+0.10} _{-0.11}	5.30 ^{+0.05} _{-0.05}	48.48 ^{+0.02} _{-0.02}	46.88 ± 0.01	4.57 ^{+0.09} _{-0.08}	3.97 ± 0.06	3.84 ^{+0.05} _{-0.05}	3.83 ± 0.02
120422A	60.87 ^{+0.24} _{-0.28}	6.54 ^{+0.12} _{-0.14}	46.06 ^{+0.03} _{-0.06}	43.81 ± 0.03	4.75 ^{+1.02} _{-1.07}	3.63 ± 0.66	5.13 ^{+0.31} _{-0.26}	5.22 ± 0.27
120521C	55.82 ^{+0.22} _{-0.18}	3.24 ^{+0.12} _{-0.09}	48.31 ^{+0.08} _{-0.05}	47.27 ± 0.03	2.33 ^{+1.66} _{-0.51}	3.12 ± 0.64	4.65 ^{+0.29} _{-0.62}	4.07 ± 0.32
130609B	66.38 ^{+0.34} _{-0.23}	6.80 ^{+0.13} _{-0.09}	49.88 ^{+0.01} _{-0.01}	48.42 ± 0.01	3.02 ^{+0.07} _{-0.05}	2.72 ± 0.04	3.52 ^{+0.03} _{-0.04}	3.61 ± 0.02
131105A	78.96 ^{+3.65} _{-3.74}	12.51 ^{+1.47} _{-1.52}	48.82 ^{+0.03} _{-0.03}	47.35 ± 0.01	4.65 ^{+0.19} _{-0.29}	4.02 ± 0.17	3.51 ^{+0.12} _{-0.08}	3.60 ± 0.07
140430A	76.29 ^{+0.75} _{-0.40}	11.32 ^{+0.31} _{-0.17}	48.29 ^{+0.03} _{-0.12}	46.75 ± 0.02	5.25 ^{+0.05} _{-0.29}	4.87 ± 0.41	3.77 ^{+0.27} _{-0.02}	3.75 ± 0.12
140703A	63.62 ^{+0.36} _{-0.18}	6.36 ^{+0.17} _{-0.09}	49.51 ^{+0.03} _{-0.04}	48.32 ± 0.01	2.13 ^{+0.14} _{-0.13}	2.17 ± 0.08	4.43 ^{+0.09} _{-0.09}	4.30 ± 0.05
160227A	58.42 ^{+0.15} _{-0.13}	3.44 ^{+0.06} _{-0.05}	48.78 ^{+0.03} _{-0.03}	47.48 ± 0.01	4.15 ^{+0.07} _{-0.07}	3.77 ± 0.10	4.45 ^{+0.08} _{-0.04}	4.37 ± 0.04
160804A	68.23 ^{+0.34} _{-0.31}	7.25 ^{+0.12} _{-0.11}	47.71 ^{+0.05} _{-0.03}	46.07 ± 0.001	5.87 ^{+0.40} _{-0.43}	5.26 ± 0.26	4.00 ^{+0.12} _{-0.14}	3.80 ± 0.07
161117A	60.83 ^{+0.11} _{-0.08}	4.96 ^{+0.05} _{-0.04}	49.07 ^{+0.03} _{-0.04}	47.58 ± 0.01	4.80 ^{+0.09} _{-0.11}	4.18 ± 0.08	3.51 ^{+0.06} _{-0.05}	3.62 ± 0.03
170113A	64.91 ^{+0.37} _{-0.38}	7.56 ^{+0.18} _{-0.18}	49.62 ^{+0.03} _{-0.02}	48.21 ± 0.01	4.71 ^{+0.07} _{-0.09}	4.17 ± 0.07	3.06 ^{+0.05} _{-0.05}	3.19 ± 0.03
170519A	67.24 ^{+0.14} _{-0.18}	7.64 ^{+0.06} _{-0.07}	48.33 ^{+0.02} _{-0.04}	46.72 ± 0.01	3.42 ^{+0.11} _{-0.19}	2.99 ± 0.12	4.06 ^{+0.08} _{-0.05}	4.07 ± 0.05
170531B	88.03 ^{+0.79} _{-0.92}	13.97 ^{+0.28} _{-0.33}	48.45 ^{+0.17} _{-0.06}	46.98 ± 0.03	4.89 ^{+1.05} _{-0.59}	4.01 ± 0.49	3.52 ^{+0.19} _{-0.50}	3.69 ± 0.17
170607A	54.63 ^{+0.06} _{-0.05}	2.80 ^{+0.02} _{-0.02}	48.01 ^{+0.02} _{-0.02}	46.27 ± 0.001	5.16 ^{+0.16} _{-0.11}	4.43 ± 0.11	4.19 ^{+0.06} _{-0.05}	4.21 ± 0.04
170705A	59.03 ^{+0.14} _{-0.08}	3.99 ^{+0.06} _{-0.03}	49.13 ^{+0.03} _{-0.03}	47.79 ± 0.01	4.70 ^{+0.09} _{-0.10}	4.28 ± 0.08	4.01 ^{+0.05} _{-0.06}	3.98 ± 0.03
171222A	59.09 ^{+0.06} _{-0.06}	3.92 ^{+0.02} _{-0.02}	47.52 ^{+0.05} _{-0.06}	46.06 ± 0.04	4.36 ^{+0.96} _{-1.32}	4.01 ± 0.91	5.25 ^{+0.39} _{-0.24}	5.10 ± 0.36
180325A	63.24 ^{+0.47} _{-0.54}	6.73 ^{+0.24} _{-0.28}	50.33 ^{+0.02} _{-0.02}	49.06 ± 0.01	2.67 ^{+0.05} _{-0.07}	2.54 ± 0.05	3.48 ^{+0.04} _{-0.03}	3.48 ± 0.03
180329B	68.27 ^{+0.49} _{-0.38}	7.93 ^{+0.20} _{-0.16}	48.87 ^{+0.02} _{-0.04}	47.41 ± 0.01	3.58 ^{+0.16} _{-0.25}	3.04 ± 0.17	3.77 ^{+0.11} _{-0.06}	3.91 ± 0.07
180404A	55.99 ^{+0.50} _{-0.43}	4.07 ^{+0.26} _{-0.22}	47.85 ^{+0.07} _{-0.06}	46.26 ± 0.02	4.71 ^{+0.68} _{-0.53}	4.10 ± 0.42	3.98 ^{+0.19} _{-0.28}	3.89 ± 0.22

this model is that there will be gamma-ray emission at the same time of the X-ray plateau phase. However, since the spectral index is $-(p - 1)/2$, the gamma-ray flux is much lower than simultaneous X-ray flux (typically $\leq 10^{-9}$ erg cm $^{-2}$ s $^{-1}$, as we can see from Figure 4). Such a low gamma-ray flux is well below the detection threshold of *Swift*-BAT and *Fermi*-GBM so that it is not easy to observe.

For those X-ray plateaus that have “internal” origins, we start from the radiation process induced by the magnetic energy dissipation within the magnetar wind to calculate the X-ray

radiation efficiency. This approach is much more realistic and reasonable than the commonly assumed constant efficiency. We have found that the X-ray radiation efficiency depends strongly on the injected luminosity. This relation has an important impact on the temporal decay index after the plateau phase, namely, making β deviate from -2 . This implies that the requirement of the braking index $n < 3$ for a $\beta < -2$ type light curve in previous studies (e.g., Zhang & Mészáros 2001; Lasky & Glampedakis 2016; Lü et al. 2018) is now largely relieved.

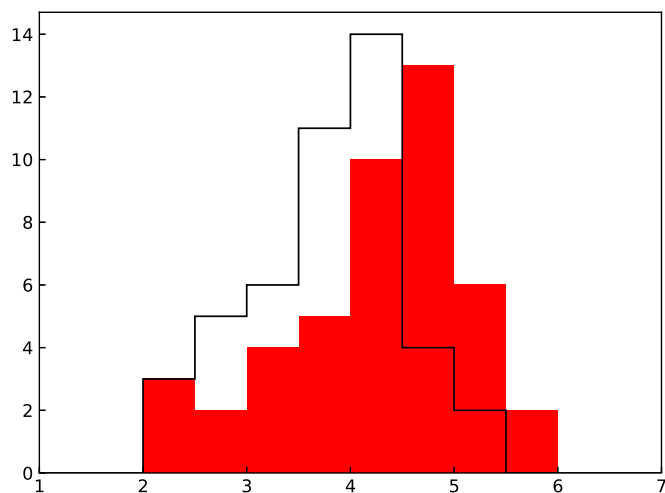


Figure 7. Comparison on the distribution of the braking index between Lü et al. (2018; black hollow histogram) and this work (red filled histogram).

Moreover, this relation has a straightforward implication that the braking index deduced from afterglow light-curve fitting should be reconsidered with care. For illustration we have adopted exactly the same sample as in Lü et al. (2018) and have redone the fitting procedure. The braking indexes are clearly larger, and the number of cases with $n < 3$ is much less than that of their work. This should be closer to reality for newborn magnetars, as k is likely to remain unchanged in such a short time ($< 10^6$ s). The effects causing an evolving k (e.g., the evolution of magnetic field strength or angle between rotation axis and dipole field axis) are expected to happen on a much longer timescale (e.g., Chen & Li 2006).

The X-ray radiation efficiency depends strongly on the saturation Lorentz factor, which is equivalent to initial magnetization (Beniamini & Giannios 2017). For a typical value of $\sigma_0 = 100$ usually adopted in a GRB study, η_X is of order 10^{-2} and much smaller than the value 0.1 usually assumed in previous studies. This means that previous studies may underestimate the initial magnetic dipole luminosity L_0 . This will in turn limit the initial spin period and magnetic field strength. In this sense, constraining σ_0 from the X-ray afterglow plateau may be possible. All of these need to be reevaluated carefully in future work.

We are grateful to Bin-Bin Zhang for providing the MCurveFit package, which is essential in generating the results of this paper. This work was supported by the National Key Research and Development Program of China (grant No. 2017YFA0402600) and the National Natural Science Foundation of China (grant Nos. 11573014, 11833003, and 11851305). D.X. was also supported by the Natural Science Foundation for the Youth of Jiangsu Province (grant No. BK20180324).

ORCID iDs

Di Xiao  <https://orcid.org/0000-0002-4304-2759>

References

- Aharonian, F. A., Bogovalov, S. V., & Khangulyan, D. 2012, *Natur*, **482**, 507
- Beniamini, P., & Giannios, D. 2017, *MNRAS*, **468**, 3202
- Beniamini, P., Giannios, D., & Metzger, B. D. 2017, *MNRAS*, **472**, 3058
- Beniamini, P., & Mochkovitch, R. 2017, *A&A*, **605**, A60
- Beniamini, P., & Piran, T. 2014, *MNRAS*, **445**, 3892
- Chen, W. C., & Li, X. D. 2006, *A&A*, **450**, L1
- Coroniti, F. V. 1990, *ApJ*, **349**, 538
- Dai, Z. G. 2004, *ApJ*, **606**, 1000
- Dai, Z. G., & Lu, T. 1998a, *A&A*, **333**, L87
- Dai, Z. G., & Lu, T. 1998b, *PhRvL*, **81**, 4301
- Dermer, C. D. 2007, *ApJ*, **664**, 384
- Drenkhahn, G. 2002, *A&A*, **387**, 714
- Drenkhahn, G., & Spruit, H. C. 2002, *A&A*, **391**, 1141
- Evans, P. A., Beardmore, A. P., Page, K. L., et al. 2009, *MNRAS*, **397**, 1177
- Genet, F., Daigne, F., & Mochkovitch, R. 2007, *MNRAS*, **381**, 732
- Giannios, D. 2012, *MNRAS*, **422**, 3092
- Giannios, D., & Spruit, H. C. 2005, *A&A*, **430**, 1
- Kluźniak, W., & Ruderman, M. 1998, *ApJL*, **508**, L113
- Kumar, P., & Zhang, B. 2015, *PhR*, **561**, 1
- Lasky, P. D., & Glampedakis, K. 2016, *MNRAS*, **458**, 1660
- Lasky, P. D., Leris, C., Rowlinson, A., & Glampedakis, K. 2017, *ApJL*, **843**, L1
- Lei, W.-H., Zhang, B., & Liang, E.-W. 2013, *ApJ*, **765**, 125
- Liang, E.-W., Zhang, B.-B., & Zhang, B. 2007, *ApJ*, **670**, 565
- Liu, T., Gu, W.-M., & Zhang, B. 2017, *NewAR*, **79**, 1
- Lü, H.-J., Lan, L., & Liang, E.-W. 2019, *ApJ*, **871**, 54
- Lü, H.-J., & Zhang, B. 2014, *ApJ*, **785**, 74
- Lyons, N., O'Brien, P. T., Zhang, B., et al. 2010, *MNRAS*, **402**, 705
- Mazzali, P. A., McFadyen, A. I., Woosley, S. E., Pian, E., & Tanaka, M. 2014, *MNRAS*, **443**, 67
- Metzger, B. D., Beniamini, P., & Giannios, D. 2018, *ApJ*, **857**, 95
- Metzger, B. D., Giannios, D., Thompson, T. A., Bucciantini, N., & Quataert, E. 2011, *MNRAS*, **413**, 2031
- Narayan, R., Piran, T., & Kumar, P. 2001, *ApJ*, **557**, 949
- Owen, B. J., Lindblom, L., Cutler, C., et al. 1998, *PhRvD*, **58**, 084020
- Panaiteescu, A., Mészáros, P., & Rees, M. J. 1998, *ApJ*, **503**, 314
- Popham, R., Woosley, S. E., & Fryer, C. 1999, *ApJ*, **518**, 356
- Rees, M. J., & Mészáros, P. 1998, *ApJL*, **496**, L1
- Rosswog, S., Ramirez-Ruiz, E., & Davies, M. B. 2003, *MNRAS*, **345**, 1077
- Rowlinson, A., O'Brien, P. T., Metzger, B. D., Tanvir, N. R., & Levan, A. J. 2013, *MNRAS*, **430**, 1061
- Rowlinson, A., O'Brien, P. T., Tanvir, N. R., et al. 2010, *MNRAS*, **409**, 531
- Ruffert, M., Janka, H.-T., Takahashi, K., & Schaefer, G. 1997, *A&A*, **319**, 122
- Shapiro, S. L., & Teukolsky, S. A. 1983, *JBA*, **93**, 276
- Spruit, H. C., Daigne, F., & Drenkhahn, G. 2001, *A&A*, **369**, 694
- Thompson, C. 1994, *MNRAS*, **270**, 480
- Troja, E., Cusumano, G., O'Brien, P. T., et al. 2007, *ApJ*, **665**, 599
- Uhm, Z. L., & Beloborodov, A. M. 2007, *ApJL*, **665**, L93
- Usov, V. V. 1992, *Natur*, **357**, 472
- Usov, V. V. 1994, *MNRAS*, **267**, 1035
- Usov, V. V. 1999, in ASP Conf. Ser. 190, Gamma-Ray Bursts: The First Three Minutes, ed. J. Poutanen & R. Svensson (San Francisco, CA: ASP), **153**
- Woosley, S. E. 1993, *ApJ*, **405**, 273
- Wu, X.-F., Gao, H., Ding, X., et al. 2014, *ApJL*, **781**, L10
- Xiao, D., & Dai, Z.-G. 2017, *ApJ*, **846**, 130
- Xiao, D., Peng, Z.-K., Zhang, B.-B., & Dai, Z.-G. 2018, *ApJ*, **867**, 52
- Yu, Y.-W., Cao, X.-F., & Zheng, X.-P. 2009, *ApJL*, **706**, L221
- Yu, Y.-W., Cheng, K. S., & Cao, X.-F. 2010, *ApJ*, **715**, 477
- Yu, Y. W., & Dai, Z. G. 2007, *A&A*, **470**, 119
- Zhang, B., Fan, Y. Z., Dyks, J., et al. 2006, *ApJ*, **642**, 354
- Zhang, B., & Mészáros, P. 2001, *ApJL*, **552**, L35
- Zhang, B., & Mészáros, P. 2002, *ApJ*, **566**, 712
- Zhang, B.-B., Uhm, Z. L., Connaughton, V., Briggs, M. S., & Zhang, B. 2016, *ApJ*, **816**, 72
- Zhang, D., & Dai, Z. G. 2008, *ApJ*, **683**, 329
- Zhang, D., & Dai, Z. G. 2009, *ApJ*, **703**, 461
- Zhang, D., & Dai, Z. G. 2010, *ApJ*, **718**, 841